ELSEVIER

Contents lists available at ScienceDirect

Applied Catalysis B: Environmental

journal homepage: www.elsevier.com/locate/apcatb





Protein-mediated synthesis of iron single atom electrocatalyst with highly accessible active sites for enhanced pH-universal oxygen reduction

Siqi Ji a,1 , Tianyang Liu b,1 , Leipeng Leng a , Hongxue Liu a , Jiangwei Zhang c , Mingyang Zhang a , Qian Xu e , Junfa Zhu e , Man Qiao f , Yu Wang b,* , J. Hugh Horton a,d,** , Zhijun Li a,*

- ^a Joint International Research Laboratory of Advanced Chemical Catalytic Materials & Surface Science, College of Chemistry and Chemical Engineering, Northeast Petroleum University, Daqing 163318, PR China
- ^b Jiangsu Collaborative Innovation Centre of Biomedical Functional Materials, School of Chemistry and Materials Science, Nanjing Normal University, Nanjing 210023, PR China
- ^c Dalian National Laboratory for Clean Energy & State Key Laboratory of Catalysis, Dalian Institute of Chemical Physics, Chinese Academy of Sciences, Dalian 116023, PR China
- ^d Department of Chemistry, Queen's University, 90 Bader Lane, Kingston K7L 3N6, Ontario, Canada
- e National Synchrotron Radiation Laboratory, University of Science and Technology of China, Hefei 230029, PR China
- f School of Chemistry and Materials Science, Nanjing University of Information Science and Technology, Nanjing 210044, PR China

ARTICLE INFO

Keywords: Single atom catalysis Iron Nitrogen-doped carbon Oxygen reduction reaction Zn-air battery

ABSTRACT

Facile synthesis of highly efficient non-precious metal electrocatalysts is intriguing as these catalysts are used in the oxygen reduction reaction (ORR). Herein, we describe an effective protein-mediated approach to access atomically dispersed iron electrocatalyst (Fe SAs/NC) with enhanced accessible metal active sites. This Fe catalyst achieves an exceptional ORR activity in the pH-universal range, especially in alkaline and acid electrolytes with half-wave potentials of 0.93 and 0.84 V (vs RHE), respectively. The unique electronic structure of Fe sites with enhanced electron/proton transportation ability contributes to the optimized adsorption/desorption of oxygen intermediates. In addition, it shows robust durability and excellent tolerance to methanol crossover in pH-universal media. Impressively, it displays encouraging performance when employed in a zinc-air battery, demonstrating a peak power density of 275.1 mW cm⁻² and a specific capacity of 753.8 mAh g⁻¹. The extremely long-term operational stability of more than 250 h further provides significant potential for its application.

1. Introduction

The electrochemical oxygen reduction reaction (ORR) is of great importance as a cathodic reaction in both rechargeable metal-air batteries and proton exchange membrane fuel cells (PEMFCs) [1,2]. However, the sluggish kinetics in the ORR severely impede the wide application of these energy storage systems [3]. Typically, highly active catalyst systems are required to substantially lower the energy barrier to drive the reaction at a low overpotential [4]. While platinum (Pt)-based materials have been long served as the state-of-the-art catalysts for ORR, the high cost, poor durability, and weak resistance to methanol/CO poisoning have greatly limited their large-scale applications [5,6]. Consequently, developing high-efficiency and low-cost ORR

electrocatalysts has been an intensive focus of research in renewable energy.

Recently, single atom catalysts (SACs) have attracted increasing interest in a variety of catalytic reactions because of their combination of well-defined active sites, maximal atomic utilization, tunable electronic/geometric properties, and the potential to bridge the gap between heterogeneous and homogeneous catalysis [7–18]. To date, a typical class of metal-nitrogen-doped carbon (M-N-C) catalysts (M typically being Fe, Co, Cu, or Mn), with high electrochemical activity, have been widely investigated and regarded as the most promising alternatives to Pt-based catalysts for ORR [3,14,19–23]. The catalytic performance of M-N-C is highly dependent on the number of exposed active sites and the porosity of the material [24–26]. These factors are strongly influenced

 $^{^{\}star}$ Corresponding authors.

^{**} Corresponding author at: Joint International Research Laboratory of Advanced Chemical Catalytic Materials & Surface Science, College of Chemistry and Chemical Engineering, Northeast Petroleum University, Daqing 163318, PR China

E-mail addresses: yu.wang@njnu.edu.cn (Y. Wang), hugh.horton@queensu.ca (J.H. Horton), zhijun.li@queensu.ca (Z. Li).

 $^{^{1}\,}$ These authors contributed equally to this work.

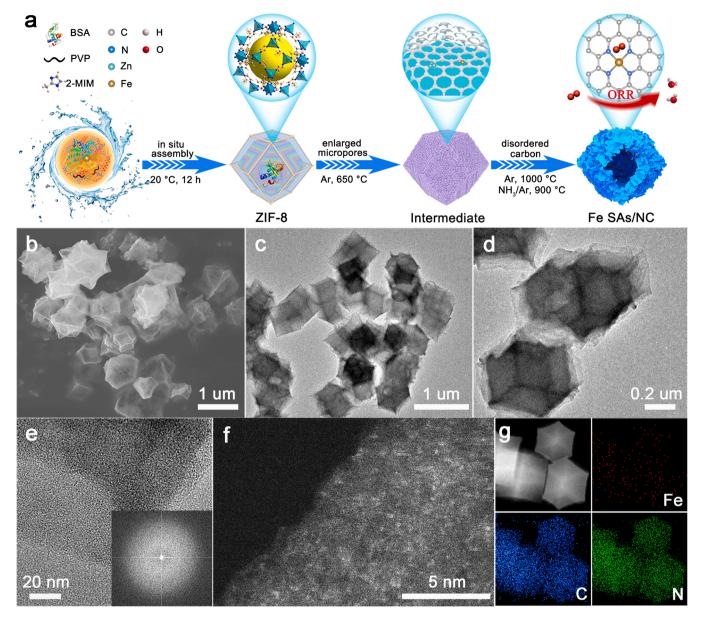


Fig. 1. Catalyst synthesis and morphology characterization. (a) Schematic illustration of the synthetic route. (b) SEM image. (c,d) TEM images, (e) HR-TEM image and SAED pattern (inset). (f) AC HAADF-STEM image. (g) EDX elemental mappings.

by the synthetic methods, yet less controllable due to the complex chemical reactions involved in the pyrolysis process. The nitrogen-doped carbon (NC) formed when zeolitic imidazolate frameworks (ZIFs) are used, contains ultrafine micropores; these inevitably create problems such as mass transfer and buried active sites inside the 3-dimensional NC matrix [24,26]. To this end, developing an effective synthetic approach to integrate highly exposed high-density active sites into a porous NC support, and simultaneously accomplish electronic and structural modulation is imperative to realize the high-performance ORR electrocatalysts that might be utilized in rechargeable Zn-air batteries.

In this work, we report a straightforward protein-mediated approach to efficiently distribute iron atoms homogeneously and in an atomically dispersed fashion across the nitrogen-doped carbon support (Fe SAs/NC). These isolated iron atoms were identified by aberration-corrected high-angle annular dark-field scanning transmission electron microscope (AC HAADF-STEM) and synchrotron X-ray absorption spectroscopy (XAFS). We show that Fe SAs/NC possesses a higher intrinsic ORR catalytic activity than that of the commercial Pt/C in pH-universal

media. This can be attributed to the unique electronic structure of Fe sites in the catalyst that weakens the binding strength of oxygen intermediates in the rate-determining step. Furthermore, a Zn-air battery based on Fe SAs/NC cathode was constructed and it exhibits high power density and robust operational stability, highlighting this method's promise for energy conversion applications.

2. Experimental sections

2.1. Synthesis of the catalysts

2.1.1. Synthesis of Fe SAs/NC

In a typical synthesis, 50 μ L of bovine serum albumin solution (50 mg/mL in deionized water), 50 μ L of PVP solution (15 mg/mL in deionized water), and 0.15 g of Fe(NO₃)₃·9H₂O were mixed with 2.232 g of Zn(NO₃)₂0.6 H₂O in 60 mL of methanol to form solution I. 2.464 g of 2-methylimidazole was dissolved in 60 mL of methanol to form solution II. Then, solution II was poured into solution I under sonication for 1 h. The mixed solution was aged at room temperature for 12 h before the

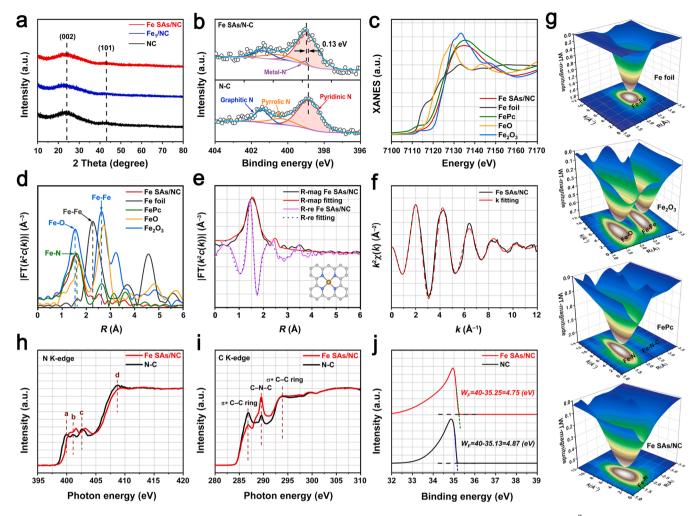


Fig. 2. Characterization of Fe SAs/NC. (a) XRD patterns. (b) High-resolution XPS N 1 s spectra. (c) Fe K-edge XANES spectra and (d) FT k^2 -weighted Fe K-edge EXAFS spectra. (e) EXAFS fitting results at K-space. (g) 3D contour WT-EXAFS plots. (h) N K-edge and (i) C K-edge XANES spectra. (j) Secondary electron tail threshold.

precipitates were collected by centrifugation and vacuum dried at 80 °C. The resulting nanocrystals were grinded and underwent a thermal treatment at 650 °C for 1 h before the temperature was increased to 1000 °C for 2 h with a heating rate of 5 °C min $^{-1}$ under an argon atmosphere in a tube furnace. When the treatment was completed and the temperature dropped to 900 °C, 5 % NH $_3$ /Ar mixed gas was introduced and kept at this temperature for 30 min. Then, the NH $_3$ /Ar mixed gas was switched to argon and the furnace was naturally cooled to room temperature. The Fe loading in the catalyst was measured to be 0.86 wt % based on the ICP-AES test.

2.1.2. Synthesis of Fe₁/NC

The synthesis of Fe_1/NC was similar to that of Fe_3/NC , except no bovine serum albumin was added. The Fe_3/NC to the catalyst was measured to be 0.71 wt% based on ICP-AES testing.

2.1.3. Synthesis of NC

The synthesis of NC was similar to that of Fe SAs/NC, except no Fe (NO₃)₃.9H₂O was added.

3. Results and discussions

3.1. Catalyst synthesis and characterizations

Here, we report a protein-mediated approach to creating atomically

dispersed iron atoms over nitrogen-doped carbon catalyst (Fe SAs/NC) for oxygen reduction reaction (ORR). The active Fe center of the catalyst coordinates with four neighboring nitrogen atoms with a Fe loading of 0.86 wt% (Table S1). In a typical synthesis (Fig. 1a), bovine serum albumin (BSA), polyvinyl pyrrolidone (PVP), metal ions, and 2-methylimidazole (2-MIM) were assembled in situ to form Fe-based BSA@ZIF-8 nanocrystals (Fig. S1). Then, two successive thermal treatments at different temperatures and atmospheres were conducted to obtain an Fe catalyst with significantly enhanced mesoporosity. This facilitates mass transportation and access to the active sites. Scanning electron microscope (SEM) and transmission electron microscope (TEM) images (Fig. 1b-d) show the typical morphology of as-prepared Fe SAs/NC. In Fig. 1e, a high-resolution TEM (HR-TEM) image reveals no nanoclusters are present over the nitrogen-doped carbon (NC) support and an amorphous structure is indicated by the ring-like selected area electron diffraction (SAED) pattern. An aberration-corrected high-angle annular dark-field scanning transmission electron microscope (AC HAADF-STEM) imaging clearly shows that atomically dispersed iron atoms are homogeneously distributed over the NC support (Fig. 1f, S2). Energydispersive X-ray elemental mapping shows the uniform distribution of Fe, C, and N elements in the catalyst (Fig. 1g). As controls, Fe₁/NC (Fe loading: 0.71 wt%) was prepared without the use of protein (Figs. S3 and S4 and Table S1) and NC was produced without addition of Fe ions (Figs. S5 and S6 and Table S1).

The X-ray diffraction (XRD) patterns suggest Fe species are highly

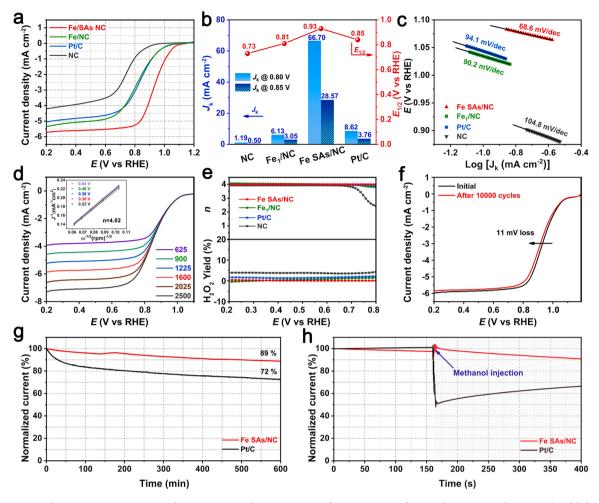


Fig. 3. ORR activity of Fe SAs/NC in 0.1 M KOH solution. (a) RDE polarization curves. (b) Comparisons of $E_{1/2}$ and J_k at 0.80 and 0.85 V. (c) Tafel slopes. (d) ORR polarization curves of Fe SAs/NC at different rotating speeds, inset shows the K–L plots. (e) Electron transfer number (n) and H_2O_2 selectivity. (f) RDE polarization curves of Fe SAs/NC before and after 10,000 potential cycles. (g) Chronoamperometric response. (h) Methanol tolerance results.

dispersed over NC support without any larger aggregates (Fig. 2a). X-ray photoelectron spectroscopy (XPS) analysis shows that the C, N, and Fe signals are observed in Fe SAs/NC (Fig. S7a). The C 1 s spectrum of Fe SAs/NC (Fig. S7b) exhibits three peaks corresponding to C-C/C=C, C=C-N, and O-C=O bonds, respectively [9,27,28]. Neither S 2p nor S 2 s signal was observed in Fe SAs/NC (Fig. S7c). This is due to the trace amount of S that exists in the catalyst, as confirmed by elemental analysis (Table S1). In the Fe 2p spectrum (Fig. S8), two dominant peaks at 711.1 and 724.6 eV are assigned to Fe $2p_{3/2}$ and Fe $2p_{1/2}$ signals, respectively, revealing the positively charged Fe species [29,30]. Notably, no zero-valent metallic Fe was detected, suggesting that the Fe atoms in the catalyst are mostly coordinated with the surrounding N or C atoms. The N 1 s spectrum in NC (Fig. 2b) is deconvoluted into pyridinic-N (398.9 eV), pyrrolic-N (400.3 eV), and graphitic-N (401.5 eV) species [29,31]. In the case of Fe SAs/NC (Table S2), the pyridinic-N peak is up-shifted 0.13 eV, along with the appearance of Fe-N signal at 399.1 eV, implying the formation of Fe-pyridinic N moieties [11,29]. The Fourier-transform infrared (FT-IR) spectra of samples are shown in Fig. S9, and typical signals of NC materials are observed [27]. The Raman spectrum of Fe SAs/NC exhibits the highest I_D/I_G ratio of 1.60 (Fig. S10), meaning the presence of a higher degree of structural defects. The electron paramagnetic resonance (EPR) spectrum of Fe SAs/NC with a sharp signal at a g value of 2.06 corresponds to the coordinatively unsaturated Fe atoms in the catalyst (Fig. S11).

The atomic dispersion and coordination environment of Fe atoms in Fe SAs/NC were further identified by X-ray absorption fine structure

(XAFS) measurements. Fig. 2c shows the X-ray absorption near-edge structure (XANES) spectra of Fe SAs/NC, Fe foil, iron phthalocyanine (FePc), FeO, and Fe₂O₃. The near edge feature of Fe SAs/NC is between those of FeO and Fe₂O₃, implying the Fe atoms in Fe SAs/NC are positively charged and the valance state is between +2 and +3 [32]. This is due to electron transfer from Fe atoms to the NC support, giving rise to a strong interaction between the metal and support. Fourier-transformed k^2 -weighted EXAFS spectra (without phase correction) are shown in Fig. 2d. Fe foil exhibits a prominent peak at 2.27 Å assigned to an Fe-Fe coordination. Fe₂O₃ shows two main peaks at 1.53 and 2.63 Å that are assigned to Fe-O and Fe—Fe coordination, respectively. In the case of Fe SAs/NC, only one dominant peak at 1.60 Å is observed which corresponds to the first coordination shell of Fe-N coordination [28]. It is similar to that of the reference FePc which has a well-defined Fe1-N4 coordinated environment. In addition, no Fe-O and Fe-Fe contributions can be found in Fe SAs/NC. The EXAFS fitting results (Fig. 2e,f and Table S3) show that the coordination number of the iron atom with its surrounding nitrogen atoms was estimated to be 4, along with an average Fe-N bond length of 1.99 Å. Wavelet transform (WT) of Fe K-edge extended X-ray absorption fine structure (EXAFS) oscillations of samples are shown in Fig. 2g. The Fe SAs/NC exhibits only one intensity maximum at 1.67 Å^{-1} , very close to that of FePc, which can be attributed to the Fe-N contribution [33]. Together, these findings strongly support the presence of atomically dispersed Fe atoms over the NC support.

Soft X-ray absorption spectroscopy (XAS) was performed to

investigate the electronic properties of N and C in samples. In the N Kedge spectra (Fig. 2h), four dominant peaks (marked a-d) are assigned to π * pyridinic N, π * pyrrolic N, π * graphitic N, and σ * C–N bonding, respectively [34]. The high-energy shift of these peaks is consistent with electron transfer between C and N following the introduction of single Fe atoms [10]. In particular, the intensity of peak a in Fe SAs/NC is relatively weaker than that of NC, implying the isolated Fe atoms are trapped at pyridine-N sites and highlighting the anchoring effect of pyridinic-N [13]. This is in line with the XPS results. The C K-edge spectra of samples (Fig. 2i) show three characteristic features of π * C–C at 286.8 eV, C–N–C at 289.5 eV, and a broad σ * C–C peak at 293.8 eV [35]. In the case of Fe SAs/NC, the intensity of C-N-C peak was increased and π * C–C ring peak was decreased significantly. This is due to electronic density change in the C-C and C-N-C lattices after doping of single Fe atoms in NC [13]. These results support the formation of metal-N bonding in Fe SAs/NC which would endow the catalyst with high conductivity and electrochemical activity. Ultraviolet photoemission spectroscopy (UPS) was conducted to investigate the energy level differences between samples. Compared to NC, the valence band of Fe SAs/NC shifts away from the Fermi level (Fig. S12). This suggests a weakened binding strength with molecular oxygen which leads to an improved ORR performance. The work functions of Fe SAs/NC and NC were calculated to be 4.75 and 4.87 eV, respectively (Fig. 2j). The smaller work function of Fe SAs/NC means higher driving energy for donating electrons from the active sites to adsorbed molecular oxygen [36], thus accelerating the formation of OOH intermediates during the ORR process. N₂ adsorption/desorption isotherms (Fig. S13) show the specific surface area of Fe SAs/NC, Fe₁/NC, and NC was measured to be 1052.6, 711.3, and 592.6 m²/g, respectively. Moreover, a significantly increased number of mesopores were observed for Fe SAs/NC and NC (Table S4). The high BET surface area and mesoporosity of Fe SAs/NC would substantially facilitate the exposure of abundant active sites and the diffusion of the reaction species.

3.2. Electrochemical oxygen reduction reaction performance

ORR activity of catalysts was examined in 0.1 M KOH solution using rotating disk electrode (RDE) measurements. Cyclic voltammetry (CV)

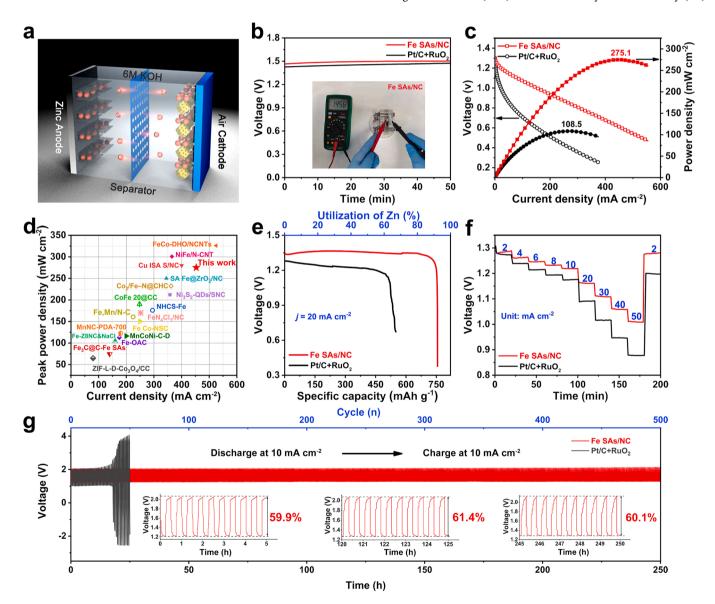


Fig. 4. Zn-air battery performance. (a) Schematic configuration of home-assembled rechargeable Zn-air battery. (b) Open-circuit plots. The inset is the OCV recorded by a multimeter. (c) Polarization and power density curves. (d) Comparison of current density and power density of Fe SAs/NC and other previously reported non-precious metal catalysts as reported in Table S7. (e) Specific capacity plots at a current density of 20 mA cm⁻². (f) Discharging curves at different current densities. (g) Galvanostatic discharge/charge cycling curves.

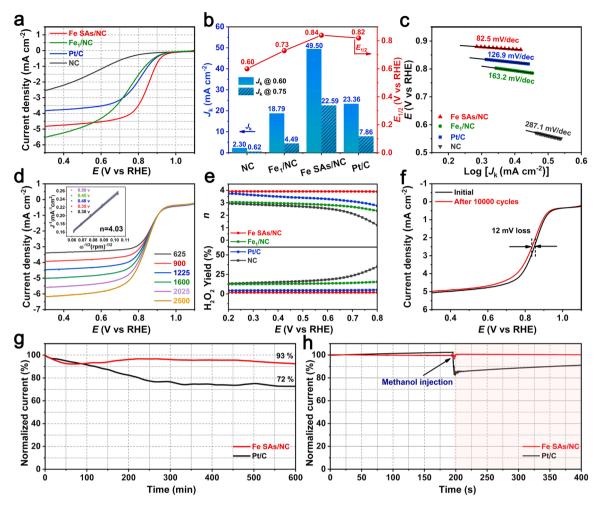


Fig. 5. ORR activity of Fe SAs/NC in 0.5 M $\rm H_2SO_4$ solution. (a) RDE polarization curves. (b) Comparison of $E_{1/2}$ and J_k at 0.60 and 0.75 V of samples. (c) Tafel slopes. (d) ORR polarization curves of Fe SAs/NC at different rotating speeds, inset is the K–L plots. (e) Electron transfer number (n) and $\rm H_2O_2$ selectivity. (f) RDE polarization curves of Fe SAs/NC before and after 10,000 potential cycles. (g) Chronoamperometric response. (h) Methanol tolerance results.

measurements were performed (Fig. S14) and oxygen reduction peaks were clearly observed for all the catalysts in O2-saturated KOH solution, but not the N2-saturated KOH solution. The optimized catalyst loading for Fe SAs/NC was determined to be 0.2 mg cm⁻² (Fig. S15). Linear sweep voltammetry (LSV) of Fe SAs/NC shows an exceptional ORR activity with an onset potential (E_{onset}) of 1.09 V versus reversible hydrogen electrode (RHE, all potentials are referenced to RHE) and a half-wave potential $(E_{1/2})$ of 0.93 V, superior to the state-of-art commercial Pt/C (E_{onset} of 1.04 V, $E_{1/2}$ of 0.85 V) and other control samples. The kinetic current densities (Jk) of samples at 0.8 and 0.85 V were calculated (Fig. 3b). As expected, Fe SAs/NC delivered the highest J_k of 66.70 and 28.57 mA cm⁻², respectively, outperforming those of NC $(1.19 \text{ and } 0.50 \text{ mA cm}^{-2})$, Fe₁/NC $(6.13 \text{ and } 3.05 \text{ mA cm}^{-2})$, and Pt/C (8.62 and 3.76 mA cm⁻²). Notably, the catalytic activity of Fe SAs/NC is among one of the best non-precious metal electrocatalysts in terms of $E_{
m onset}$ and $E_{1/2}$ in alkaline conditions (Table S5). For example, Jiang et al. described a dual protection strategy to prepare a Fe_{SA}-N-C catalyst for ORR [37]; however, merely $E_{\rm onset}$ of 0.99 V and $E_{1/2}$ of 0.9 V were obtained in 0.1 M KOH. Li et al. reported a highly active and stable Fe single atom catalyst with a high loading of 2.16 wt% [38], but its ORR performance (E_{onset} of 0.986 V; $E_{1/2}$ of 0.9 V) is inferior to that of our Fe SAs/NC catalyst. The outstanding ORR kinetics of Fe SAs/NC was further evidenced by a smaller Tafel slope of 68.6 mV dec⁻¹ relative to those of $104.8 \text{ mV} \text{ dec}^{-1}$ for NC, $90.2 \text{ mV} \text{ dec}^{-1}$ for Fe_1/NC , and 94.1 mV dec^{-1} for Pt/C (Fig. 3c). The electrochemical active surface area (ECSA) of these samples was investigated by evaluating the

electrochemical double-layer capacitance (Cdl). As shown in Fig. S16, S17, the C_{dl} of Fe SAs/NC (9.6 mF cm⁻²) is higher than those of NC (3.4 mF cm $^{-2}$), Fe₁/NC (5.1 mF cm $^{-2}$), and Pt/C (8.2 mF cm $^{-2}$), meaning the Fe SAs/NC possesses a higher density of electroactive sites. The electrochemical impedance spectroscopy (EIS) Nyquist plot of Fe SAs/NC (Fig. S18, Table S6) exhibits a smaller semicircle than those of the control samples, suggesting that the active catalyst exhibits the lowest charge transfer resistance. To assess the ORR pathway of Fe SAs/NC, RDE measurements at rotation rates ranging from 625 to 2500 rpm were performed (Fig. 3d). According to the K-L equation, the electron-transfer number (n) is calculated to be 4.02, close to the theoretical value of 4 for the 4e ORR process. Rotating ring disk electrode (RRDE) tests further confirm the 4e⁻ transfer process and the H₂O₂ yield of Fe SAs/NC is below 0.8 % over the potential range of 0.2-0.8 V (Fig. 3e). These results unambiguously validate a highly efficient 4e-ORR pathway of Fe SAs/NC with a negligible H₂O₂ side product.

Durability and methanol tolerance are two critical issues for the practical application of ORR electrocatalysts. To evaluate the catalytic durability, Fe SAs/NC was subjected to continuous cycling at a scan rate of 100 mV between 0.75 and 1.10 V in 0.1 M KOH. As shown in Fig. 3f, no significant activity decay in $E_{1/2}$ (\sim 11 mV) is observed after 10,000 continuous potential cycles, implying excellent ORR stability. Detailed examination of the catalyst after the durability test displays no observable change in morphology, demonstrating excellent structural stability (Fig. S19). Additionally, under a constant potential of 0.6 V (Fig. 3g), the current density of Fe SAs/NC retained \sim 89 % of its initial value after

10 h, outperforming that of the commercial Pt/C catalyst ($\sim 72~\%$ retained). The methanol tolerance results show Fe SAs/NC maintains a relatively stable current density following the methanol injection (Fig. 3h); however, the Pt/C displays a sharp drop in current density due to the methanol oxidation. The LSV curves of Fe SAs/NC in 0.1 M KOH with and without methanol addition also suggest excellent methanol tolerance ability (Fig. S20). To confirm the significant role of atomically dispersed Fe sites in the catalyst on ORR activity, KSCN was used to block these Fe sites. The Fe SAs/NC (Fig. S21) exhibits a significant activity decay in $E_{1/2}$ (32 mV) following KSCN addition, confirming the key role of these isolated Fe sites in ORR. These results provide evidence of the excellent ORR performance of Fe SAs/NC under alkaline conditions.

Electrochemical OER measurements were further performed in 0.1 M KOH solution (Fig. S22) to evaluate the electrocatalytic performance of Fe SAs/NC, with Fe₁/NC, NC, and commercial RuO₂ catalysts as references. As shown in Fig. S22a,b, the electrocatalytic activity of NC is negligible compared to other metal-based catalysts. The benchmark RuO₂ catalyst exhibited the smallest overpotential of 296 mV to afford the current density of 10 mA cm⁻². In the case of Fe SAs/NC, it demonstrated an overpotential of 358 mV. Compared to NC (597 mV), this significantly enhanced electrocatalytic activity of Fe SAs/NC verified the strong electronic interactions between Fe sites and NC support, which are beneficial for OER. The Fe₁/NC showed a lower catalytic activity with a high overpotential of 455 mV when compared with that of Fe SAs/NC. This suggests the significant role of incorporating protein during the synthetic process. Then, Tafel plots of these catalysts were investigated to obtain insights into the OER kinetics (Fig. S22c). The benchmark RuO₂ catalyst displayed the smallest Tafel slope of 86.9 mV/ dec, followed by 109.7 mV/dec of Fe SAs/NC, 120.6 mV/dec of Fe₁/NC, and 206.1 mV/dec of NC. Moreover, the Fe SAs/NC demonstrated excellent OER durability with a negligible activity decay (~ 8 mV) following 1000 repeated cycles (Fig. S22d). Overall, these findings demonstrate the Fe SAs/NC catalyst can efficiently catalyze OER and the Fe1-N4 moieties served as the metal active sites.

Having demonstrated exceptional ORR activity for the Fe SAs/NC catalyst under alkaline conditions, we proceeded with the investigation of the catalyst's potential when incorporated in an aqueous zinc-air battery (ZAB), as shown in Fig. 4a. A mixed Pt/C+RuO₂ catalyst (mass ratio: 1:1) was employed as a control. The battery loaded with Fe SAs/ NC (Fig. 4b) exhibits a high open-circuit voltage (OCV) of 1.46 V, larger than that of the Pt/C+RuO₂ counterpart (1.41 V). Polarization curves were recorded to evaluate the corresponding output power density of catalysts assembled in ZABs (Figs. S23 and 4c). In the case of Fe SAs/NC, a peak power density of 275.1 mW cm⁻² was obtained at a current density of 538 mA cm $^{-2}$, significantly higher than that of ZAB (Pt/C+RuO₂) (108.5 mW cm $^{-2}$ at 281 mA cm $^{-2}$). Remarkably, the Fe SAs/ NC-based battery achieved excellent performance compared with previously reported benchmarking non-precious metal electrocatalysts (Fig. 4d and Table S7). As shown in Fig. 4e, the specific capacity of ZAB (Fe SAs/NC) at a discharge current of 20 mA cm⁻² was determined to be 753.8 mAh g⁻¹, significantly higher than that of 521.9 mAh g⁻¹ for ZAB (Pt/C+RuO₂). Accordingly, the Zn utilization ratio for ZAB (Fe SAs/NC) and ZAB (Pt/C+RuO2) was calculated to be 91.9 % and 63.6 %, respectively, based on theoretical capacity (~820 mAh g⁻¹). Fig. 4f shows the discharge curves of batteries at current densities between 2 and 50 mA cm⁻². The results demonstrate that the voltage value of a Fe SAs/NC-based battery can be recovered without activity decay, demonstrating excellent ORR activity and reversibility. Rechargeability and cyclic durability of catalysts were investigated under continuous galvanostatic discharge-charge at a current density of 10 mA cm⁻² (Fig. 4g). Unlike the Pt/C+RuO2-assembled battery, the Fe SAs/NCbased battery delivered negligible voltage fading within 250 h (500 charging/discharging cycles), validating the exceptional long-term durability. Moreover, it exhibits a high round-trip efficiency (initial: 59.9 %; intermediate: 61.4 %; final: 60.1 %) during the entire recycling

process. Together, these findings demonstrate the great potential of Fe SAs/NC for use in zinc-air batteries.

ORR activity of catalysts was further examined in a more challenging acidic condition (0.5 M H₂SO₄). The LSV results (Fig. 5a) of Fe SAs/NC achieved the highest ORR activity with E_{onset} of 1.01 V and $E_{1/2}$ of 0.84 V, both of which are more positive than those of the Pt/C (0.98 and 0.82 V) and other control samples. The J_k of catalysts at 0.60 and 0.75 V were calculated and are shown in Fig. 5b. Notably, the Fe SAs/NC delivered the highest J_k of 49.50 and 22.59 mA cm⁻², respectively, exceeding those of NC (2.30 and 0.62 mA cm $^{-2}$), Fe₁/NC (18.79 and 4.49 mA cm^{-2}), and Pt/C (23.36 and 7.86 mA cm⁻²). The smaller Tafel slope of Fe SAs/NC (82.5 mV dec⁻¹) when compared with those of NC $(287.1 \text{ mV dec}^{-1})$, Fe_1/NC $(163.2 \text{ mV dec}^{-1})$, and Pt/C (126.9 mV)dec⁻¹) reveals its outstanding ORR kinetics (Fig. 5c). The catalytic activity of Fe SAs/NC in acid conditions is among one of the best observed to date in non-precious metal electrocatalyst systems (Table S8). For example, Huang et al. fabricated a single Fe site catalyst by a doublelayer MOF strategy and it demonstrated excellent ORR performance in 0.5 M H₂SO₄ with E_{onset} and $E_{1/2}$ being 0.91 V and 0.781 V, respectively [28]. The ECSA of catalysts in 0.5 M H₂SO₄ solution was studied (Figs. S24 and S25) and the C_{dl} of Fe SAs/NC showed the highest value of 29.2 mF cm⁻², followed by Fe₁/NC (11.8 mF cm⁻²), Pt/C (10.0 mF cm⁻²), and NC (4.8 mF cm⁻²). Based on the K-L equation, the n was determined to be 4.03 for Fe SAs/NC (Fig. 5d). The RRDE results (Fig. 5e) further validate the 4e ORR process and the negligible H₂O₂ yield for Fe SAs/NC (below 0.7 % over the scanned potential range). Excitingly, no significant activity decay in $E_{1/2}$ (~12 mV) is observed for Fe SAs/NC after 10,000 continuous potential cycles (Fig. 5f). Furthermore, the current density of Fe SAs/NC retained ~ 93 % of the initial value under a constant potential of 0.6 V after 10 h (Fig. 5g), superior to that of the commercial Pt/C catalyst (\sim 72 % retained). KSCN poisoning tests demonstrate the critical role of single Fe atoms in the catalyst (Fig. S26). Especially, after the addition of KSCN into 0.5 M H₂SO₄, the E_{onset} and $E_{1/2}$ of Fe SAs/NC exhibit a negative shift and a decreased diffuse-limited current density. Following a water rinsing step, the ORR performance of Fe SAs/NC was recovered when tested in 0.1 M KOH, which is due to the dissociation of SCN on the Fe sites under alkaline conditions.

Having demonstrated excellent ORR performance of Fe SAs/NC under both acidic and alkaline conditions, we next set out to explore its ORR activity in neutral conditions (Fig. S27). Gratifyingly, Fe SAs/NC achieved the highest ORR activity with $E_{\rm onset}$ of 0.93 V and $E_{1/2}$ of 0.65 V, outperforming those of Pt/C (0.93 and 0.62 V) and other control samples (Fig. S27a). It delivered the highest J_k of 17.57 mA cm⁻² at 0.55 V (Fig. S27b), exceeding those of NC (0.90 mA cm⁻²), Fe₁/NC $(6.02 \text{ mA cm}^{-2})$, and Pt/C (9.45 mA cm⁻²). Moreover, it achieved the smallest Tafel slope of 137.2 mV dec⁻¹ compared with these controls (Fig. S28). Moreover, its ORR performance was comparable to most of the previously reported Fe-based electrocatalysts in 0.1 M PBS (Table S9). Wang and co-workers developed a Fe single atom catalyst (Fe,N/PGC-30) and it manifested an ORR with E_{onset} of 0.85 V and $E_{1/2}$ of 0.61 V [39], inferior to our Fe SAs/NC catalyst. Under a constant potential of 0.6 V, the current density of Fe SAs/NC retained \sim 85 % of the initial value after 10 h (Fig. S29), superior to that of the commercial Pt/C catalyst ($\sim 66 \%$ retained). It also demonstrated superior methanol tolerance than that of Pt/C in neutral conditions (Fig. S30).

For the universality of this protein-mediated approach, different metal salts and protein—human serum albumin (HSA) were employed (Fig. S31). We observe that this approach is effective for these metal salts and HSA, but systematic optimization works for other types of proteins and metal salts are ongoing in our laboratory to uncover this point thoroughly.

3.3. DFT calculations

Density functional theory (DFT) calculations were further performed

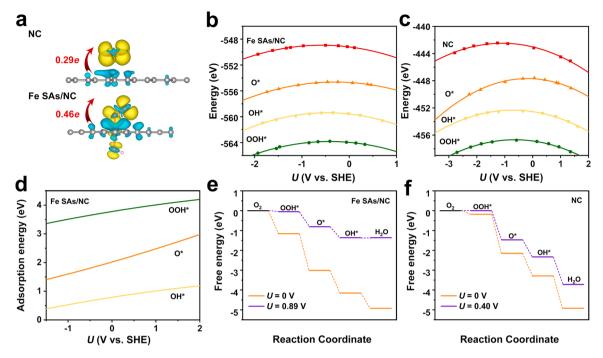


Fig. 6. Density functional theory calculations via a constant-potential approach. (a) Differential charge density of molecular oxygen adsorbed on NC and Fe SAs/NC (isosurface is 0.001 e/Å^3). The charge accumulation and depletion are colored in yellow and cyan. The quadratic functions of the electrode potential and the total energy for (b) Fe SAs/NC and (c) NC derived from the calculations with different system charges. (d) Adsorption energies of OOH*, O*, and OH* intermediates on Fe SAs/NC as a function of potential. ORR free energy diagrams of (e) Fe SAs/NC and (f) NC at zero and limiting potentials.

to investigate the intrinsic electrocatalytic activity of Fe SAs/NC for ORR. Based on previous works, the Fe site in FeN₄ moiety is preferentially covered with an intrinsic intermediate OH*, with the formation of Fe(OH)N₄ moiety to facilitate intermediate binding. Hence, the Fe(OH) N₄ moiety was adopted in the present study [5,15]. As shown in Fig. 6a and S32, the differential charge density in Fe SAs/NC shows the electrons transfer between Fe (depletion) and O₂ (accumulation), with 0.46e obtained by molecular oxygen. In sharp contrast, only 0.29e was noticed for NC (Fig. 6a and S33). Of note is that the O₂ adsorption on NC is relatively weak when compared with Fe SAs/NC. The higher amount of e transferred from the catalyst would substantially facilitate the activated O species to be reduced to OOH* and further transformed to O* and OH*. This is in line with the UPS results.

To provide a reasonable description of the effect of the electrode potential on electrocatalysis, we applied a constant-potential method to explore the activity of Fe SAs/NC and NC toward the electrochemical ORR [40–42]. For each reaction species, nine independent calculations with system charge values from -2e to 2e in a charge step of 0.5e were performed. The optimized structures of O_2 * , OOH* , O* , and OH* on Fe SAs/NC and NC are shown in Figs. S34 and S35. From these calculations, the relationship between electrode potential and total free energy of each species was established (Fig. 6b,c); the adsorption free energy values of intermediates were determined accordingly (Fig. 6d, \$36). Our calculations suggest that the last electrochemical step (the reduction of OH* to H2O) is the rate-limiting step for the Fe SAs/NC catalyst, while that of NC alone is the first electrochemical step (the reduction of O2 to OOH*) due to its poor O2 activation ability (Fig. 6e,f and Table S10). Specifically, the limiting potential (U_L) of the Fe SAs/NC catalyst (0.89 V) is much higher than that of NC (0.40 V), indicating that the Fe single atom sites have great potential for facilitating the ORR. Overall, these findings suggest the Fe SAs/NC possesses excellent ORR catalytic activity, in good agreement with the experimental results.

4. Conclusion

In summary, we report a facile protein-mediated approach to

constructing a single Fe atom catalyst supported over NC with abundant N anchoring sites. The as-prepared catalyst possesses significantly higher specific surface area and mesoporosity to facilitate the mass transport and exposure of active Fe sites. Moreover, due to the compositional and coordinational merits as well as the optimized electronic metal-support interactions, this Fe catalyst exhibits exceptional ORR activity, durability, and tolerance to methanol crossover in pH-universal media, superior to the commercial Pt/C catalysts. Noteworthy, this catalyst affords excellent performance for rechargeable Zn–air battery. DFT calculations reveal that the Fe $_1$ N4 moieties served as the active sites to significantly lower the energy barrier for the rate-limiting step, thus giving rise to the enhanced intrinsic ORR catalytic activity. This protein-mediate approach paves a way for the rational design of single atom electrocatalysts for energy conversion.

CRediT authorship contribution statement

Siqi Ji: Investigation, Methodology, Validation, Writing – original draft. Tianyang: Methodology, Validation. Leipeng Leng: Formal analysis. Hongxue Liu: Validation. Jiangwei Zhang: Validation. Mingyang Zhang: Validation. Qian Xu: Methodology. Junfa Zhu: Software. Man Qiao: Software. Yu Wang: Investigation. J. Hugh Horton: Supervision, Writing – review & editing. Zhijun Li: Conceptualization, Funding acquisition, Methodology, Project administration, Supervision, Writing – review & editing.

Declaration of Competing Interest

The authors declare that they have no known competing financial interests or personal relationships that could have appeared to influence the work reported in this paper.

Data Availability

The authors do not have permission to share data.

Acknowledgments

This work was supported by the China Postdoctoral Science Foundation (2019M661247, 2020T130091), Program for Overseas Talents Introduction of Northeast Petroleum University (15041260303), and Heilongjiang Touyan Innovation Team Program.

Appendix A. Supporting information

Supplementary data associated with this article can be found in the online version at doi:10.1016/j.apcatb.2022.121987.

References

- M.K. Debe, Electrocatalyst approaches and challenges for automotive fuel cells, Nature 486 (2012) 43–51.
- [2] M. Li, X. Bi, R. Wang, Y. Li, G. Jiang, L. Li, C. Zhong, Z. Chen, J. Lu, Relating catalysis between fuel cell and metal-air batteries, Matter 2 (2020) 32–49.
- [3] F. Cheng, J. Chen, Metal-air batteries: from oxygen reduction electrochemistry to cathode catalysts, Chem. Soc. Rev. 41 (2012) 2172–2192.
- [4] Z.W. Seh, J. Kibsgaard, C.F. Dickens, I. Chorkendorff, J.K. Norskov, T.F. Jaramillo, Combining theory and experiment in electrocatalysis: insights into materials design, Science 355 (2017) 6321.
- [5] H.T. Chung, D.A. Cullen, D. Higgins, B.T. Sneed, E.F. Holby, K.L. More, P. Zelenay, Direct atomic-level insight into the active sites of a high-performance PGM-free ORR catalyst, Science 357 (2017) 479–484.
- [6] A.A. Gewirth, J.A. Varnell, A.M. DiAscro, Nonprecious metal catalysts for oxygen reduction in heterogeneous aqueous systems, Chem. Rev. 118 (2018) 2313–2339.
- [7] X. Li, Y. Huang, B. Liu, Catalyst: single-atom catalysis: directing the way toward the nature of catalysis, Chem 5 (2019) 2733–2735.
- [8] Z. Li, Y. Chen, X. Lu, H. Li, L. Leng, T. Zhang, J.H. Horton, Synthesis of cobalt single atom catalyst by a solid-state transformation strategy for direct C-C cross-coupling of primary and secondary alcohols, Nano Res. 15 (2022) 4023–4031.
- [9] Z. Li, T. Fan, H. Li, X. Lu, S. Ji, J. Zhang, J.H. Horton, Q. Xu, J. Zhu, Atomically defined undercoordinated copper active sites over nitrogen-doped carbon for aerobic oxidation of alcohols, Small 18 (2022), 2106614.
- [10] H. Su, W. Zhou, W. Zhou, Y. Li, L. Zheng, H. Zhang, M. Liu, X. Zhang, X. Sun, Y. Xu, F. Hu, J. Zhang, T. Hu, Q. Liu, S. Wei, In-situ spectroscopic observation of dynamic-coupling oxygen on atomically dispersed iridium electrocatalyst for acidic water oxidation, Nat. Commun. 12 (2021) 6118.
- [11] H. Tian, X. Cui, H. Dong, G. Meng, F. Kong, Y. Chen, L. Peng, C. Chen, Z. Chang, J. Shi, Engineering single MnN₄ atomic active sites on polydopamine-modified helical carbon tubes towards efficient oxygen reduction, Energy Storage Mater. 37 (2021) 274–282.
- [12] Z. Li, D. Wang, Y. Wu, Y. Li, Recent advances in the precise control of isolated single-site catalysts by chemical methods, Natl. Sci. Rev. 5 (2018) 673–689.
- [13] T. Cui, L. Ma, S. Wang, C. Ye, X. Liang, Z. Zhang, G. Meng, L. Zheng, H.S. Hu, J. Zhang, H. Duan, D. Wang, Y. Li, Atomically dispersed Pt-N₃C₁ sites enabling efficient and selective electrocatalytic C-C bond cleavage in lignin models under ambient conditions, J. Am. Chem. Soc. 143 (2021) 9429–9439.
- [14] X. Wang, Z. Li, Y. Qu, T. Yuan, W. Wang, Y. Wu, Y. Li, Review of metal catalysts for oxygen reduction reaction: from nanoscale engineering to atomic design, Chem 5 (2019) 1486–1511.
- [15] Y. Wang, Y.J. Tang, K. Zhou, Self-adjusting activity induced by intrinsic reaction intermediate in Fe-N-C single-atom catalysts, J. Am. Chem. Soc. 141 (2019) 14115–14119.
- [16] Z. Li, L. Leng, X. Lu, M. Zhang, Q. Xu, J.H. Horton, J. Zhu, Single palladium atoms stabilized by β-FeOOH nanorod with superior performance for selective hydrogenation of cinnamaldehyde, Nano Res. 15 (2021) 3114–3121.
- [17] Z. Li, X. Lu, W. Sun, L. Leng, M. Zhang, H. Li, L. Bai, D. Yuan, J.H. Horton, Q. Xu, J. Wang, One-step synthesis of single palladium atoms in WO_{2,72} with high efficiency in chemoselective hydrodeoxygenation of vanillin, Appl. Catal. B Environ. 298 (2021), 120535.
- [18] Z. Li, W. Wei, H. Li, S. Li, L. Leng, M. Zhang, J.H. Horton, D. Wang, W. Sun, C. Guo, W. Wu, J. Wang, Low-temperature synthesis of single palladium atoms supported on defective hexagonal boron nitride nanosheet for chemoselective hydrogenation of cinnamaldehyde, ACS Nano 15 (2021) 10175–10184.
- [19] Y. Wang, H. Su, Y. He, L. Li, S. Zhu, H. Shen, P. Xie, X. Fu, G. Zhou, C. Feng, D. Zhao, F. Xiao, X. Zhu, Y. Zeng, M. Shao, S. Chen, G. Wu, J. Zeng, C. Wang, Advanced electrocatalysts with single-metal-atom active sites, Chem. Rev. 120 (2020) 12217–12314.
- [20] M. Arif Khan, C. Sun, J. Cai, D. Ye, K. Zhao, G. Zhang, S. Shi, L. Ali Shah, J. Fang, C. Yang, H. Zhao, S. Mu, J. Zhang, Potassium-ion activating formation of Fe-N-C moiety as efficient oxygen electrocatalyst for Zn-Air batteries, ChemElectroChem 8 (2021) 1298–1306.

- [21] L. Shi, X. Lin, F. Liu, Y. Long, R. Cheng, C. Tan, L. Yang, C. Hu, S. Zhao, D. Liu, Geometrically deformed iron-based single-atom catalysts for high-performance acidic proton exchange membrane fuel cells, ACS Catal. 12 (2022) 5397–5406.
- [22] X. Tan, H. Li, W. Zhang, K. Jiang, S. Zhai, W. Zhang, N. Chen, H. Li, Z. Li, Square-pyramidal Fe-N₄ with defect-modulated O-coordination: two-tier electronic structure fine-tuning for enhanced oxygen reduction, Chem. Catal. 2 (2022) 816-835.
- [23] Z. Li, L. Leng, S. Ji, M. Zhang, H. Liu, J. Gao, J. Zhang, J.H. Horton, Q. Xu, J. Zhu, Engineering the morphology and electronic structure of atomic cobalt-nitrogencarbon catalyst with highly accessible active sites for enhanced oxygen reduction, J. Energy Chem. 73 (2022) 469–477.
- [24] H. Zhou, T. Yang, Z. Kou, L. Shen, Y. Zhao, Z. Wang, X. Wang, Z. Yang, J. Du, J. Xu, M. Chen, L. Tian, W. Guo, Q. Wang, H. Lv, W. Chen, X. Hong, J. Luo, D. He, Y. Wu, Negative pressure pyrolysis induced highly accessible single sites dispersed on 3D graphene frameworks for enhanced oxygen reduction, Angew. Chem. Int. Ed. 59 (2020) 20465–20469.
- [25] T. Zhou, H. Shan, H. Yu, C. Zhong, J. Ge, N. Zhang, W. Chu, W. Yan, Q. Xu, H. Wu, C. Wu, Y. Xie, Nanopore confinement of electrocatalysts optimizing triple transport for an ultrahigh-power-density zinc-air fuel cell with robust stability, Adv. Mater. 32 (2020), 2003251.
- [26] X. Wan, X. Liu, Y. Li, R. Yu, L. Zheng, W. Yan, H. Wang, M. Xu, J. Shui, Fe-N-C electrocatalyst with dense active sites and efficient mass transport for high-performance proton exchange membrane fuel cells, Nat. Catal. 2 (2019) 259–268.
- [27] Y. Xiong, J. Dong, Z.Q. Huang, P. Xin, W. Chen, Y. Wang, Z. Li, Z. Jin, W. Xing, Z. Zhuang, J. Ye, X. Wei, R. Cao, L. Gu, S. Sun, L. Zhuang, X. Chen, H. Yang, C. Chen, Q. Peng, C.R. Chang, D. Wang, Y. Li, Single-atom Rh/N-doped carbon electrocatalyst for formic acid oxidation, Nat. Nanotechnol. 15 (2020) 390–397.
- [28] M. Zhao, H. Liu, H. Zhang, W. Chen, H. Sun, Z. Wang, B. Zhang, L. Song, Y. Yang, C. Ma, Y. Han, W. Huang, A. pH-universal, ORR catalyst with single-atom iron sites derived from a double-layer MOF for superior flexible quasi-solid-state rechargeable Zn-air batteries, Energy Environ. Sci. 14 (2021) 6455–6463.
- [29] Z. Wang, X. Jin, C. Zhu, Y. Liu, H. Tan, R. Ku, Y. Zhang, L. Zhou, Z. Liu, S.J. Hwang, H.J. Fan, Atomically dispersed Co₂-N₆ and Fe-N₄ costructures boost oxygen reduction reaction in both alkaline and acidic media, Adv. Mater. 33 (2021), 2104718.
- [30] K. Yuan, D. Lutzenkirchen-Hecht, L. Li, L. Shuai, Y. Li, R. Cao, M. Qiu, X. Zhuang, M.K.H. Leung, Y. Chen, U. Scherf, Boosting oxygen reduction of single iron active sites via geometric and electronic engineering: nitrogen and phosphorus dual coordination, J. Am. Chem. Soc. 142 (2020) 2404–2412.
- [31] Y. Wu, C. Ye, L. Yu, Y. Liu, J. Huang, J. Bi, L. Xue, J. Sun, J. Yang, W. Zhang, X. Wang, P. Xiong, J. Zhu, Soft template-directed interlayer confinement synthesis of a Fe-Co dual single-atom catalyst for Zn-air batteries, Energy Storage Mater. 45 (2022) 805–813.
- [32] X. Zhong, S. Ye, J. Tang, Y. Zhu, D. Wu, M. Gu, H. Pan, B. Xu, Engineering Pt and Fe dual-metal single atoms anchored on nitrogen-doped carbon with high activity and durability towards oxygen reduction reaction for zinc-air battery, Appl. Catal. B Environ. 286 (2021), 119891.
- [33] J. Feng, R. Cai, E. Magliocca, H. Luo, L. Higgins, G.L.F. Romario, X. Liang, A. Pedersen, Z. Xu, Z. Guo, A. Periasamy, D. Brett, T.S. Miller, S.J. Haigh, B. Mishra, M.M. Titirici, Iron, nitrogen Co-doped carbon spheres as low cost, scalable electrocatalysts for the oxygen reduction reaction, Adv. Funct. Mater. 31 (2021), 2102974.
- [34] T. Sun, W. Zang, H. Yan, J. Li, Z. Zhang, Y. Bu, W. Chen, J. Wang, J. Lu, C. Su, Engineering the coordination environment of single cobalt atoms for efficient oxygen reduction and hydrogen evolution reactions, ACS Catal. 11 (2021) 4498–4509.
- [35] S. Liu, Y. Zhang, B. Ge, F. Zheng, N. Zhang, M. Zuo, Y. Yang, Q. Chen, Constructing graphitic-nitrogen-bonded pentagons in interlayer-expanded graphene matrix toward carbon-based electrocatalysts for acidic oxygen reduction reaction, Adv. Mater. 33 (2021), 2103133.
- [36] P. Peng, L. Shi, F. Huo, C. Mi, X. Wu, S. Zhang, Z. Xiang, A pyrolysis-free path toward superiorly catalytic nitrogen-coordinated single atom, Sci. Adv. 5 (2019) eaaw2322
- [37] L. Jiao, R. Zhang, G. Wan, W. Yang, X. Wan, H. Zhou, J. Shui, S.H. Yu, H.L. Jiang, Nanocasting SiO₂ into metal-organic frameworks imparts dual protection to highloading Fe single-atom electrocatalysts, Nat. Commun. 11 (2020) 2831.
- [38] Y. Chen, S. Ji, Y. Wang, J. Dong, W. Chen, Z. Li, R. Shen, L. Zheng, Z. Zhuang, D. Wang, Y. Li, Isolated single iron atoms anchored on N-doped porous carbon as an efficient electrocatalyst for the oxygen reduction reaction, Angew. Chem. Int. Ed. 56 (2017) 6937–6941.
- [39] W. Gu, L. Hu, J. Li, E. Wang, Iron and nitrogen co-doped hierarchical porous graphitic carbon for a high-efficiency oxygen reduction reaction in a wide range of pH, J. Mater. Chem. A 4 (2016) 14364–14370.
- [40] Z. Duan, G. Henkelman, Theoretical resolution of the exceptional oxygen reduction activity of Au(100) in alkaline media, ACS Catal. 9 (2019) 5567–5573.
- [41] J.S. Filhol, M. Neurock, Elucidation of the electrochemical activation of water over Pd by first principles, Angew. Chem. Int. Ed. 45 (2006) 402–406.
- [42] Y. Wang, L. You, K. Zhou, Origin of the N-coordinated single-atom Ni sites in heterogeneous electrocatalysts for CO₂ reduction reaction, Chem. Sci. 12 (2021) 14065–14073.